Applied Catalysis B: Environmental 183 (2016) 133–141

Contents lists available at ScienceDirect

Applied Catalysis B: Environmental

journal homepage: www.elsevier.com/locate/apcatb

A stable Ag_3PO_4@g-C_3N_4 hybrid core@shell composite with enhanced visible light photocatalytic degradation

Li Liu, Yuehong Qi, Jinrong Lu, Shuanglong Lin, Weijia An, Yinghua Liang, Wenquan Cui*

College of Chemical Engineering, North China University of Science and Technology, Tangshan 063009, PR China

ARTICLE INFO

Article history:
Received 26 July 2015
Received in revised form 11 October 2015
Accepted 18 October 2015
Available online 21 October 2015

Keywords:
Photocatalysis
Ag_3PO_4@g-C_3N_4
Core@shell
Degradation
Stability

ABSTRACT

Ag_3PO_4@g-C_3N_4 core@shell composites were prepared via an ultrasonication/chemisorption method. The degradation of methylene blue (MB) over Ag_3PO_4@g-C_3N_4 composites was investigated to evaluate their photocatalytic performance. The Ag_3PO_4@g-C_3N_4 sample presented the best photocatalytic activity, degrading 97% MB after irradiation for 30 min. Superior stability was also observed in the cyclic runs. The composite has excellent photocatalytic activity and photo-stability and the optimal content of g-C_3N_4 in the composites is 7.0 wt.%. The efficient photo-generated charge separation originated from a strong interaction in the intimately contact interface, which was confirmed by the results of photocurrent and EIS measurements. Based on the experimental results, a photocatalytic mechanism for organics degradation over Ag_3PO_4@g-C_3N_4 photocatalysts was proposed.

1. Introduction

Semiconductor photocatalysis can be used to decompose various organic compounds in open air under aqueous conditions with solar energy. It has become one of the most important technologies for environmental remediation [1]. The traditional photocatalyst TiO_2 can only absorb UV light which only accounts for 4% of the total sunlight and thus significantly limits its practical applications in the utilizing of solar light [2,3]. Therefore, new and more efficient visible-light-driven (VLD) photocatalysts are strongly desired for the effective harvest of solar energy.

Ag_3PO_4 photocatalysts have attracted considerable attentions due to their excellent visible-light-driven photocatalytic activity for the degradation of organic pollutants and broad band gap of 2.45 eV [4]. The quantum yield of oxygen generated from the water oxidation catalyzed by Ag_3PO_4 under visible light can reach as high as 90%, which is significantly higher than the ~20% yield produced by most other photocatalysts under the same conditions [5]. In addition, Ag_3PO_4-based composite photocatalysts have high visible light absorption and can suppress the recombination of photo-generated charge carriers. For example, Ag_3PO_4/TiO_2 [6], Ag_3PO_4/ZnO [7] and Ag_3PO_4/AgI [5] composite photocatalysts can effectively accelerate the separation of photo-generated charge carriers due to their strong electric field at the interface and wide band-edge offset. However, two factors lead to the instability for Ag_3PO_4 as the photocatalyst in the process of the photocatalytic reaction. Firstly, Ag_3PO_4 could be photo-corroded and decomposed into the silver with low activities during the photocatalytic reactions, which limits the recycle and efficiency of the Ag_3PO_4 composite photocatalysts [8]. Secondly, Ag_3PO_4 photocatalyst possesses a relatively higher Ksp of 1.6×10^{-16} compared with other photocatalysts such as CdS (Ksp 8.0×10^{-27}) and Cu_2S (Ksp 2.5×10^{-48}), so Ag_3PO_4 photocatalyst could slightly dissolute as Ag^+ and PO_4^{3-} in aqueous solution [9]. Many reports revealed that the photocatalytic activity and stability of Ag_3PO_4 can be improved by being combined with GO [10], rGO [11] and g-C_3N_4 [12,13], due to the acceleration of photo-induced charge separation. However, these point contact between the bulk phases usually leads to low conjunction of Ag_3PO_4 with semiconductors, which could significantly limit the photo-induced charge separation. Photocatalysts with core@shell nanostructures possess excellent visible-light-driven photocatalytic activity and many other advantages [14–16]. The stabilizing material sheets coated on the surface of Ag_3PO_4 nanoparticles can protect Ag_3PO_4 from dissolution in aqueous solution, thus enhance the structural stability of Ag_3PO_4-based core@shell photocatalysts during the photocatalytic reaction [17]. The large contact area between core and shell can facilitate the separation of the photo-generated charge carriers at their interface. In addition, its coupling with semiconductors can form a strong electric field at the interface near the band-edge offset, which can

* Corresponding author. Fax: +86 315 2592169.
E-mail address: wkcui@163.com (W. Cui).

http://dx.doi.org/10.1016/j.apcatb.2015.10.035
0926-3373/

significantly accelerate the transfer of photo-generated charge carriers. Therefore, the shell materials that can facilitate the charge transfer and separation are strongly desired.

g-C_3N_4 nano-sheet is a well-known π-conjugated material in the improvement of the photo-generated electron-hole pair separation [18]. More importantly, it is profoundly tolerant to temperature and chemicals due to its s-triazine ring structure and high condensation [19]. g-C_3N_4 nano-sheet is a soft polymer, and thus can be used as a coating material for other compounds [20–22]. Zhu and co-workers [16,22] reported that the improved stability and photocatalytic performance of Ag and ZnO could were obtained by coating g-C_3N_4 nano-sheet as a shell layer, due to the strong interface interaction accelerating the transfer of photo-generated charge, and the protective shield prevent the contact between core materials and aqueous solution.

In the present work, we reported a novel stable Ag_3PO_4@g-C_3N_4 core@shell composite photocatalyst by an ultrasonication/chemisorption method. The result suggests the shell g-C_3N_4 can protect Ag_3PO_4 from dissolution in aqueous solution, thus enhance the structural stability of Ag_3PO_4. Meanwhile, a strong interaction in the intimately contact interface and well-aligned band-structures make the photo-induced electrons in the LUMO of g-C_3N_4 injected into CB of Ag_3PO_4 and photo-induced hole in the VB of Ag_3PO_4 injected into the HOMO of g-C_3N_4, which effectively transfer the charge. This synergistic effect resulting in the photo-corrosion of Ag_3PO_4 was suppressed and generated dramatic visible photocatalytic activity and photo-stability. The possible mechanisms of photo-corrosion inhibition and enhancement of photocatalytic activity have been established in detail.

2. Experimental

2.1. Synthesis of g-C_3N_4

The g-C_3N_4 power was synthesized according to a procedure reported in the literature [22]. Briefly, 10 g of melamine was put into an alumina crucible with a cover, heated to 550 °C at a heating rate of 2 °C min^{-1} in a muffle furnace and maintained at 550 °C for 4 h. All experiments were performed in air. The yellow product was collected and ground into powder for further use.

The g-C_3N_4 nano-sheets were obtained by liquid exfoliating of as-prepared bulk g-C_3N_4 in water. In detail, 50 mg of bulk g-C_3N_4 powder dispersed in 50 mL water and then ultrasound for about 24 h. The initial formed suspension was then centrifuged at about 2000 rmp to remove the residual un-exfoliated g-C_3N_4. Finally, the suspension of ultrathin g-C_3N_4 nano-sheets was used for further study.

2.2. Synthesis of Ag_3PO_4

Ag_3PO_4 was prepared by a precipitation method. Briefly, 2.0 g PVP was suspended in 150 mL distilled water, followed by the addition of 2.4 g $AgNO_3$. Na_2HPO_4 solution was prepared by dissolving 0.84 g Na_2HPO_4 in 20 mL distilled water and added to the PVP-$AgNO_3$ aqueous solution dropwise under stirring. The mixture solution was stirred for 1 h and centrifuged. The precipitate was collected, washed with water and ethanol for 3 times and dried at 60 °C for 12 h.

2.3. Synthesis of Ag_3PO_4@g-C_3N_4

The concentration of ultra-thin g-C_3N_4 nano-sheets suspension was estimated to be about 0.12 mg/mL. A certain amount of Ag_3PO_4 was added to the ultrathin g-C_3N_4 nano-sheets dispersion (100 mL) and stirred for 48 h. The nominal weight ratios of g-C_3N_4 to Ag_3PO_4 were 1, 5, 7, 9 and 10 wt%, and weight of Ag_3PO_4 was 1.2 g, 0.24 g, 0.17 g, 0.13 g and 0.12 g, respectively. The water was evaporated and the residue was dried at 60 °C for 24 h to obtain an Ag_3PO_4@g-C_3N_4 composite powder. The sample named M-Ag_3PO_4@g-C_3N_4 (7 wt.%) was prepared by the direct mechanical mixing of Ag_3PO_4 and g-C_3N_4 (7 wt.%) in an agate mortar.

2.4. Characterization of photocatalysts

The crystal structures and phase states of Ag_3PO_4@g-C_3N_4 composites were determined by X-ray diffractometry (XRD) using a Rigaku D/MAX2500 PC diffractometer with Cu Kα radiation at an operating voltage of 40 kV and an operating current of 100 mA. The morphologies of the samples were imaged with a scanning electron microscopy (SEM) (Hitachi, s-4800) and a transmission electron microscopy (TEM) (JEOL Ltd., JEM-2010). UV–vis (UV–Vis) diffuse reflectance spectra were recorded on a UV–vis spectrometer (Puxi, UV1901). The Fourier transform infrared spectra (FTIR) of the samples were recorded on an IR Vertex70 FTIR spectrometer. Raman spectra were recorded on a microscopic confocal Raman spectrometer (Thermo Electron DXR) with an excitation of 785 nm laser light. Electrochemical and photoelectrochemical measurements were performed in 0.1 M Na_2SO_4 electrolyte solution in a three-electrode quartz cell. Pt sheet was used as a counter electrode and Hg/Hg_2Cl_2/sat. KCl was used as a reference electrode. The Ag_3PO_4@g-C_3N_4 composite thin film on indium-tin oxide (ITO) was used as the working electrode for investigation. The photoelectrochemical response was recorded with a CHI 660B electrochemical system.

2.5. Photocatalytic activity

The photocatalytic activities of Ag_3PO_4@g-C_3N_4 composites were evaluated with its catalytic degradation of MB under irradiation of visible light. A 250 W halide lamp (Philips) with a 420 nm cutoff filter was located at a distance of 10 cm from an unsealed beaker for the first test group. A glass reactor with 25 ± 2 °C circulating water flowing outside was employed for the secondary test group. For each test, 0.05 g catalyst powder was added into 100 mL 10 mg/L MB solution. The test solutions were stirred in the dark for 30 min before irradiated under the visible light. During the irradiation, a 3 mL sample of the reaction suspension was taken every 3 min and centrifuged at 10,000 rpm for 6 min. The supernatant was collected and analyzed on the UV–vis spectrophotometer.

Photocatalytic degradations of MB in the dark in the presence of the photocatalyst and under visible-light irradiation in the absence of the photocatalyst were also used as negative controls. In addition, the degradation of bisphenol A (BPA) was investigated with the same procedure except that concentrations BPA in each test solution were determined with HPLC.

3. Results and discussion

The crystal structure and phase composition of the Ag_3PO_4@g-C_3N_4 photocatalysts were determined with XRD. Fig. 1 shows the XRD patterns of g-C_3N_4, g-C_3N_4 nanosheets, Ag_3PO_4 and Ag_3PO_4@g-C_3N_4 photocatalysts. Two characteristic peaks were observed in the XRD spectra of bulk g-C_3N_4. The peak at 13.1° can be assigned to the in-plane structural packing motif of tris-triazine units and is indexed as the (1 0 0) peak. Another strong peak at 27.5° is ascribed to the interlayer stacking of aromatic segments with a d = 0.324 nm and is indexed as the (0 0 2) peak of the conjugated aromatic stacking [23]. Only one peak of (0 0 2) was observed in XRD spectra of the g-C_3N_4 nano-sheets films, indicating that the interlayer structure was broken by the exfoliation [24]. All the diffraction peaks of Ag_3PO_4@g-C_3N_4 composites with various g-C_3N_4 contents can be readily indexed to the body-centered

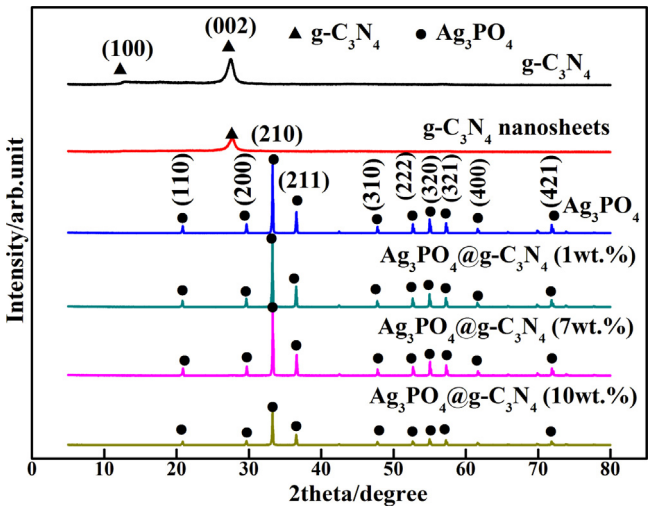

Fig. 1. XRD patterns of g-C_3N_4, g-C_3N_4 nano-sheets, Ag_3PO_4, and Ag_3PO_4@g-C_3N_4 photocatalysts.

cubic structure of Ag_3PO_4 (JCPDS No. 06-0505). No characteristic diffraction peaks for g-C_3N_4 were observed in its XRD spectra pattern due to its low content in the composite. The presence of g-C_3N_4 was confirmed by FT-IR and Raman analyses when its content was increased to 7 wt.% as described below.

The morphologies, crystal phases and compositions of the products were determined by SEM and TEM. As can be seen, the bulk g-C_3N_4 is composed of micrometer size solid agglomerates (Fig. 2a). It became loose and soft agglomerate nano-sheets after it was exfoliated and flakes with laminar morphology were observed (Fig. 2b). As shown in its TEM image (Fig. 2c), the g-C_3N_4 nano-sheet contains a layer structure with some chiffon-like ripples and wrinkles. To gain the thickness of the nano-sheets after the ultrasonic exfoliation, atomic force microscopy (AFM) images were recorded. The thickness of g-C_3N_4 nano-sheets after ultrasonic treatment was around 1.5 nm (Fig. 2j), which was consistent with the literature for the few layer g-C_3N_4 nano-sheets [24]. The Ag_3PO_4 particles are 200–300 nm regular spheres (Fig. 2d). Fig. 2e and f are the high-magnification SEM images of the Ag_3PO_4@g-C_3N_4 core@shell composite. It can be seen clearly that the composite is composed of well-defined nano-spheres distinctly enwrapped with gauze-like g-C_3N_4 nano-sheets. From TEM image (Fig. 2g and h) of the composite, the outer layer of the as-prepared Ag_3PO_4@g-C_3N_4 sample is distinctly different from the Ag_3PO_4 core. The high-resolution TEM images in Fig. 2i prove it further. These Ag_3PO_4 nanoparticles were in intimate contact with the g-C_3N_4, and the lattice fringes of Ag_3PO_4 can be clearly identified in the Fig. 2i. The lattice fringes of nanoparticles have a spacing of 0.27 nm, which is in agreement with the spacing of the (2 1 0) planes of Ag_3PO_4 and consistent with JCPDS card no. 06-0505 [25,26]. Compared with point contact structure of traditional composite materials, the core@shell Ag_3PO_4@g-C_3N_4 on three-dimensional structure has a larger contact area, which can promote photo-induced charge separation. The preparation pathway of Ag_3PO_4@g-C_3N_4 hybrid structure is shown in Fig. 3. First, the s-triazine ring structure of layered material g-C_3N_4 was prepared by heating melamine to 550 °C. Then, g-C_3N_4 is exfoliated into sheet structures through an ultrasonic method in H_2O solvent. Experimental studies show that the g-C_3N_4 thin nano-sheets can be kept for a long period of time in water without precipitation occurred. The core@shell structure of g-C_3N_4 and Ag_3PO_4 was formed by the incubation of the g-C_3N_4 with Ag_3PO_4 particles for 48 h, which minimized the surface energy.

The UV–vis absorption spectra of Ag_3PO_4, g-C_3N_4 and the Ag_3PO_4@g-C_3N_4 composite are shown in Fig. 4. The light absorption edge of pure Ag_3PO_4 is 530 nm, corresponding to a band gap (Eg) of 2.45 eV [4] and that of pure g-C_3N_4 is ~470 nm, corresponding to a band gap (Eg) of 2.64 eV. An evident hypochromic shift of photo-absorption edge from 470 nm to 460 nm was observed in the UV–vis absorption spectrum of g-C_3N_4 nano-sheets [24,27]. Therefore, the ultrathin g-C_3N_4 nano-sheet is more photo-responsive

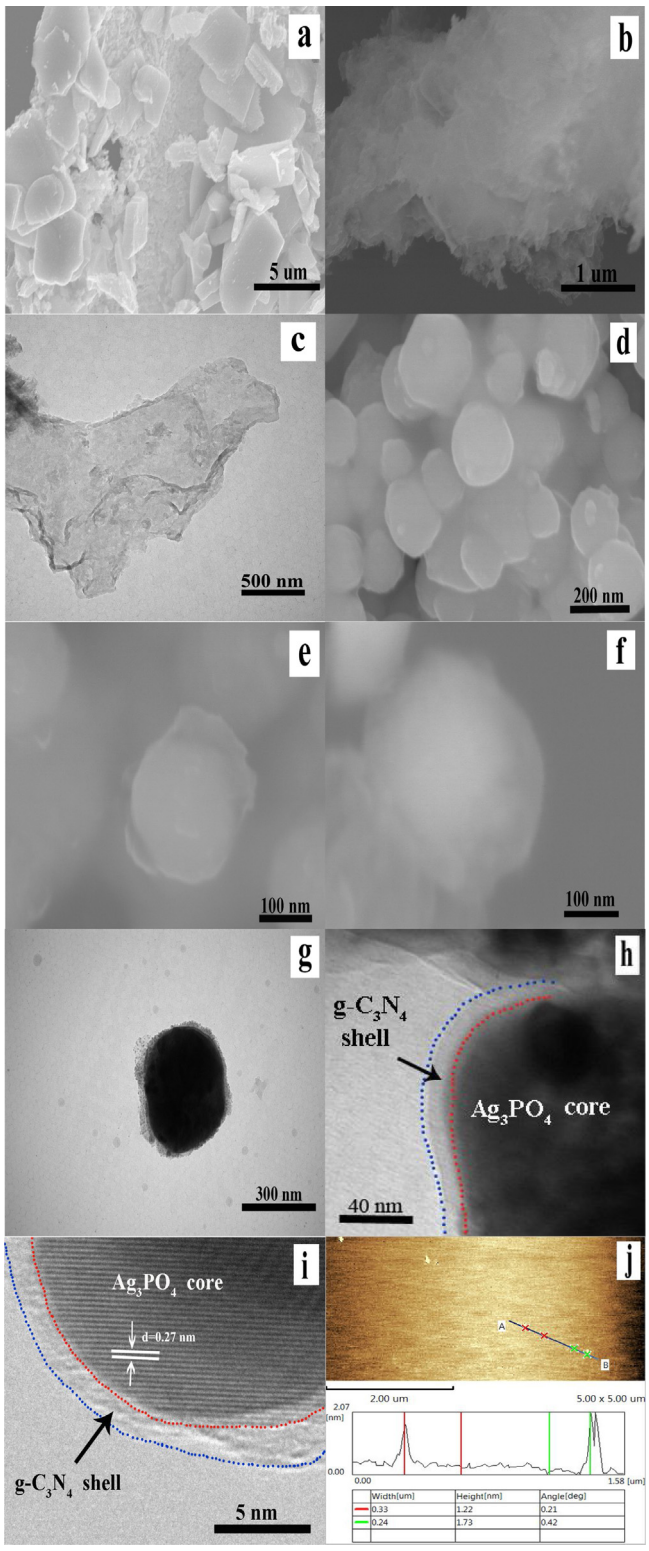

Fig. 2. SEM images of g-C_3N_4 (a) and g-C_3N_4 nanosheets (b), TEM images of g-C_3N_4 nanosheets(c) SEM images of Ag_3PO_4 (d), Ag_3PO_4@g-C_3N_4 (e and f), TEM (g, h) and HRTEM (j) images of Ag_3PO_4@g-C_3N_4, AFM of g-C_3N_4 nanosheets (j).

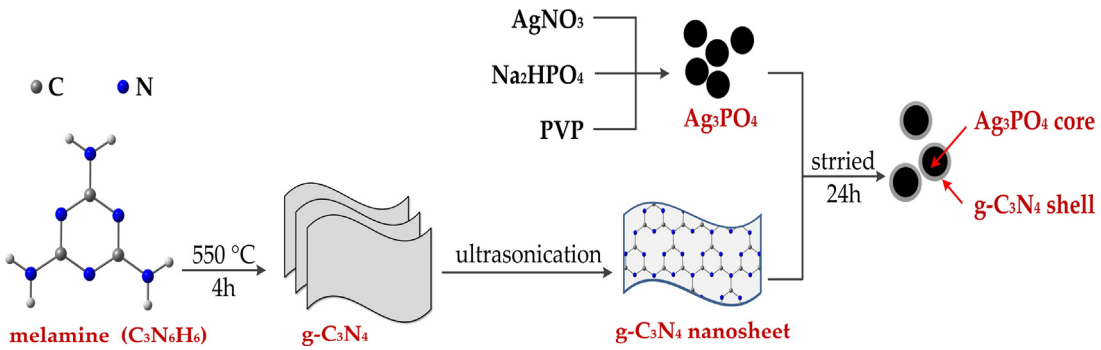

Fig. 3. The schematic illustration of the preparation of Ag_3PO_4@g-C_3N_4 composites.

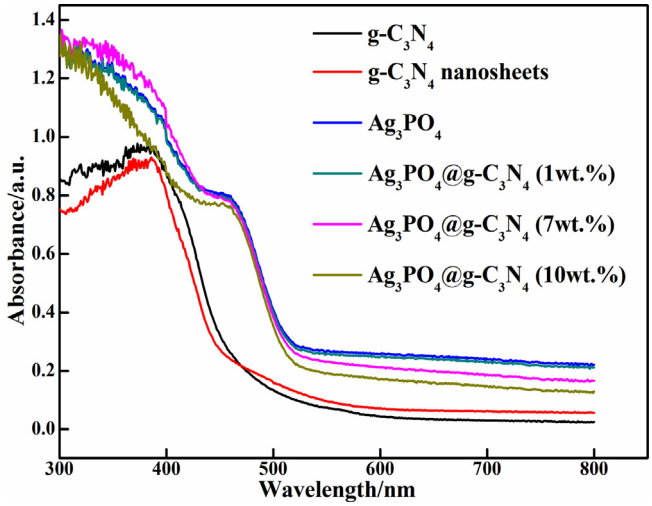

Fig. 4. UV–vis diffuse reflectance spectra of Ag_3PO_4, g-C_3N_4 and the Ag_3PO_4@g-C_3N_4 photocatalysts.

than the bulk g-C_3N_4, which was further demonstrated by its color change varied from yellow to white. The absorption edge of Ag_3PO_4 changed slightly after modified with g-C_3N_4. The Ag_3PO_4@g-C_3N_4 composite showed significantly stronger light absorption than g-C_3N_4.

The Fourier transform infrared spectrometry (FTIR) spectra of g-C_3N_4, Ag_3PO_4 and Ag3PO4@g-C3N4 composite photo-catalyst are shown in Fig. 5. The two peaks at 1010 cm^{-1} and 558 cm^{-1} in the FTIR spectrum of Ag_3PO_4 were assigned to the P—O stretching vibration in PO_4. The bands at 1659 and 1381 cm^{-1} can be ascribed to the stretching and bending of H—O in the water adsorbed on its surface [28–30]. The water molecules and hydroxyl groups adsorbed on the Ag_3PO_4 surface can be conversed to hydroxyl free radicals in the photocatalytic reaction for the oxidation of organic pollutants. The strong absorption band of 1200–1700 cm^{-1}, with the characteristic peaks at 1240 and 1640 cm^{-1}, in the FTIR spectrum of pure g-C_3N_4, can be attributed to the typical stretching vibration of CN heterocycles [31]. The absorption peak at 808 cm^{-1} is attributed to the breathing of the triazine units [31]. The IR spectrum of as-exfoliated g-C_3N_4 nano-sheets have almost identical absorption pattern with that of the bulk g-C_3N_4, indicating there is no functional groups emerged during its exfoliation process. In the Ag_3PO_4@g-C_3N_4 composite, all of these bands moved to lower wavenumber as shown in the Fig. 5b. The red shift of these bands suggested that the bond strengths of C=N and C—N were weakened so that the g-C_3N_4 conjugated bond was stretched and a more widely conjugated chain containing g-C_3N_4 and Ag_3PO_4 had already appeared [32–34]. Compared with the point contact, the core@shell structure owning a large contact area is more conducive to the formation of the interaction. This interaction was essential to promoting the separation efficiency of photo-generated carriers and enhancing photocatalytic activity and anti-photocorrosion performance.

Raman spectroscopy analysis was further carried out to confirm the presence of g-C_3N_4 in the Ag_3PO_4@g-C_3N_4 composites. Fig. 6 is the Raman spectra of Ag_3PO_4, g-C_3N_4 and Ag_3PO_4@g-C_3N_4 composite. The strong absorption peak at 912 cm^{-1} in the spectrum of Ag_3PO_4 can be assigned to the motion of terminal oxygen bond vibration of its phosphate group [35]. The distinct Raman peak at 567 cm^{-1} is ascribed to the symmetric stretch of P—O—P bonds. For the Raman spectra of g-C_3N_4, the as-exfoliated g-C_3N_4 nano-sheets showed identical raman shifts with that of bulk g-C_3N_4, indicating the exfoliated ultrathin g-C_3N_4 nano-sheets retain the same crystal structure of bulk g-C_3N_4 [27]. The characteristic peaks of the C—N extended network at 472, 707, 767, 978, 1233 and 1312 cm^{-1} are consistent with those obtained from pristine CN in literature [36]. All characteristic bands of Ag_3PO_4 were observed in the Roman spectrum of Ag_3PO_4@g-C_3N_4 composite. However, the intensities of characteristic absorption peaks of g-C_3N_4 were decreased dramatically and some of peaks even disappeared in the Roman spectrum of Ag_3PO_4@g-C_3N_4 composite, indicating the reduction of g-C_3N_4 during the preparation of Ag_3PO_4@g-C_3N_4 composite.

To compare the photocatalytic activities of Ag_3PO_4 before and after coated with g-C_3N_4, a series of photocatalytic degradation experiments were performed using methyl blue (MB) as a model pollutant under visible light irradiation. As shown in Fig. 7a, MB was only slightly degraded in the absence of catalyst (blank reaction in Fig. 7a) or in the presence of catalyst in dark (dark in Fig. 7a), indicating that the blank photolytic degradation was negligible. Nearly 97% of MB was degraded with 30 min irradiation in the presence of Ag_3PO_4@g-C_3N_4 photocatalyst, indicating its excellent photocatalystic activity. The photocatalyst prepared by simply mechanically mixing Ag_3PO_4 and g-C_3N_4 (7 wt.%) together in an agate mortar only degraded 79% of MB under same conditions. Only 69% MB was degraded by pure Ag_3PO_4 under visible light irradiation in 30 min. The MB degradation in the presence of g-C_3N_4 was also investigated under same conditions. These results indicate that Ag_3PO_4@g-C_3N_4 core@shell composite is a much better photocatalyst than pure Ag_3PO_4, g-C_3N_4 and M-Ag_3PO_4@g-C_3N_4 (7 wt.%). In the present work, the degradation of BPA over Ag_3PO_4@g-C_3N_4 under visible light irradiation (>420 nm) was also studied to further evaluate the photocatalytic performance of Ag_3PO_4@g-C_3N_4 composites. As can be seen from Fig. 7b, BPA was degraded 57.2% over Ag_3PO_4 under visual light irradiation for 30 min. The degradation ratio was significantly increased to 94.6% over the Ag_3PO_4@g-C_3N_4 composite photocatalyst with a 30 min visible light irradiation. These results indicate that Ag_3PO_4@g-C_3N_4 can be used for the removal of

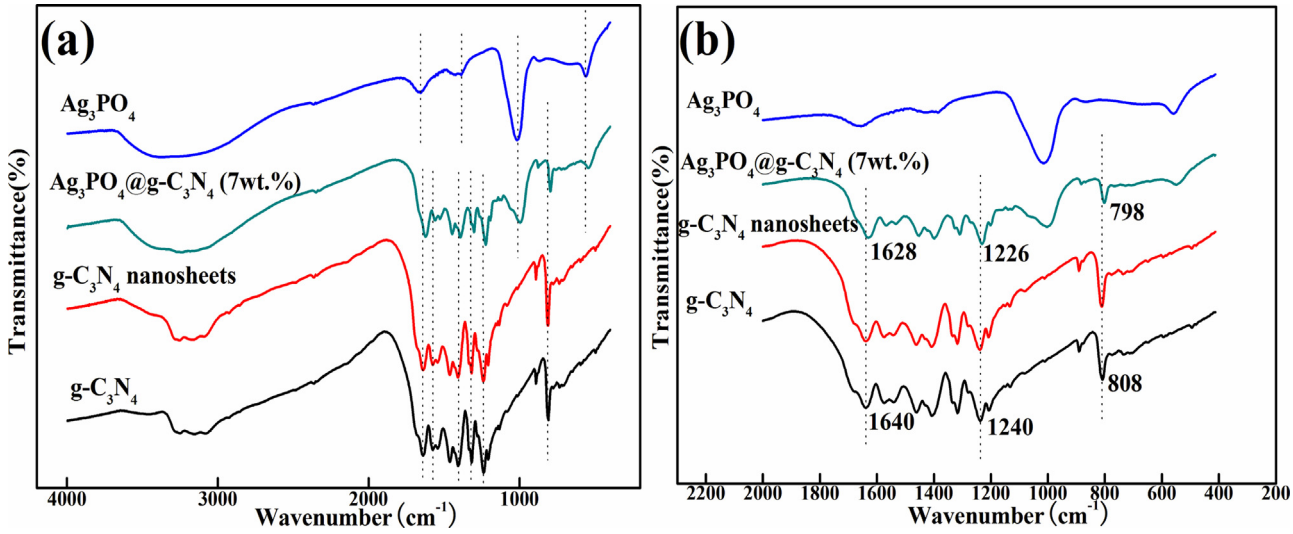

Fig. 5. FTIR spectra of Ag_3PO_4, g-C_3N_4, g-C_3N_4 nanosheets and Ag_3PO_4@g-C_3N_4 (7 wt.%).

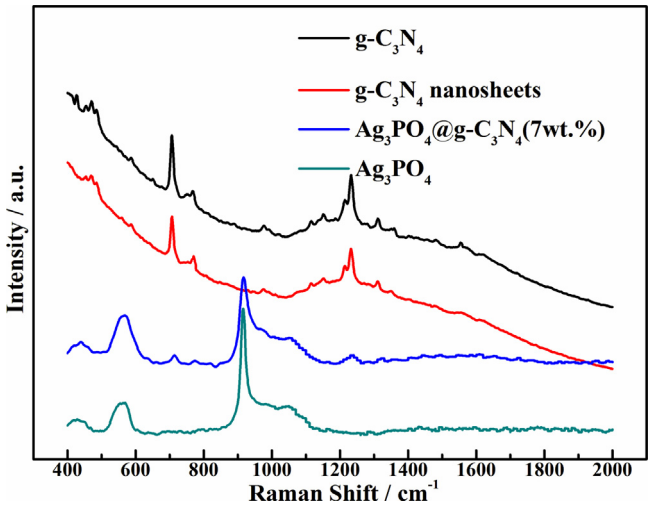

Fig. 6. Raman spectra of Ag_3PO_4, g-C_3N_4 and Ag_3PO_4@g-C_3N_4 (7 wt.%).

BPA and the decomposition of BPA molecules results from photocatalytic degradation instead of physical adsorption. Well-aligned band-structures and the strong interaction in the intimately contact interface enhance charge separation, which result in excellent photocatalytic activity.

Next, we investigated the effect of g-C_3N_4 content on the photocatalytic activity of Ag_3PO_4@g-C_3N_4 composites. Fig. 8 was degradation rate (a) and first-order rate constant (b) of Ag_3PO_4@g-C_3N_4 composite. The photocatalytic performance was significantly improved after the introduction of g-C_3N_4 and increased with the increase of g-C_3N_4 content from 1.0 to 7.0 wt.%. For example, the Ag_3PO_4@g-C_3N_4 composite containing 7.0 wt.% g-C_3N_4 degraded 97% of MB and showed a photodegraded rate constant of 0.117 min^{-1}, representing an optimal coating contribution to the high photocatalytic activity (Fig. 8). Further increasing the g-C_3N_4 content to 10 wt.% in the composite leads to a decreased photocatalytic activity (Fig. 7). It also could be seen from the graph of Fig. 8 that the coating amount of g-C_3N_4 had a great influence on the photocatalytic activity of the as-prepared samples. When the g-C_3N_4 content was relatively low (<7.0 wt.%), the contact area gradually increased with the increment of g-C_3N_4. In this case, an effective charge separation can be achieved, resulting in enhancement of photocatalytic activity and inhibition of photo-corrosion. Alternatively, when the g-C_3N_4 content is relatively high (>7.0 wt.%), it might be explained that large amount of g-C_3N_4 forms a thick completely closed shell on the Ag_3PO_4 nano-spheres, which suppress the electrons on the enriched Ag_3PO_4 transfer to surface of g-C_3N_4. In this case, it reduces the number of hydroxyl radical which can act a dominant reactive species in the photocatalytic degradation. At the same time, this can facilitate the recombination of photoinduced electron-hole pairs. Consequently, the photocatalytic activity will decrease rapidly with further increasing of the g-C_3N_4 content.

The electrons and holes produced by photocatalysis have strong reduction and oxidation capacities. The main active species of different photocatalysts may vary due to their different band structure and phase compositions. Therefore, different scavenges used as probes were introduced into the photocatalytic degradation of RhB in order to determine the relative roles of the reactive species. In the present work, EDTA-2Na and iso-propyle alcohol (IPA) were introduced into the photocatalytic degradation system of MB as holes and hydroxyl radical scavenges, respectively, to determine the roles of the reactive species. If the free radical scavenged played acted an important role in the photocatalytic degradation of MB, the rate constant (k_{app}) would be reduced greatly in the presence of the appropriate scavenger. Before irradiation, the scavenger (10 mmol/L) was added to the MB solutions together with the catalyst. As depicted in Fig. 9, the degradation rate decreases obviously to 16.9% in the presence of EDTA-2Na (h^+ scavenger) and the degradation rate was 97% in the absence of scavengers, which suggests that h^+ is the main reactive species for MB degradation(Fig. 9a). The introduction of IPA showed a significant effect on the k_{app} which can decreased obviously from 0.117 min^{-1} to 0.020 min^{-1} (Fig. 9b), suggesting that radical was also a dominant reactive species. The results indicate that superoxide radicals, direct holes and hydroxyl radical are active species for the photocatalytic degradation.

The stability of a photocatalyst is important for its assessment and application. The recycling runs of MB degradation over Ag_3PO_4 and Ag_3PO_4@g-C_3N_4 (7 wt.%) composite were performed to evaluate their photocatalytic stability. As shown in Fig. 10a, the degradation over bare Ag_3PO_4 decreased from 69% to 27% after five recycling runs. In contrast, the 81% MB was degraded over Ag_3PO_4@g-C_3N_4 composite after 5 recycling runs, indicating its high stability in the photocatalytic reaction under visible-light irradiation. The g-C_3N_4 nano-sheets coated on the surface of Ag_3PO_4 nanoparticles can effectively protect it from dissolution in the aqueous solution, which can significantly increase the

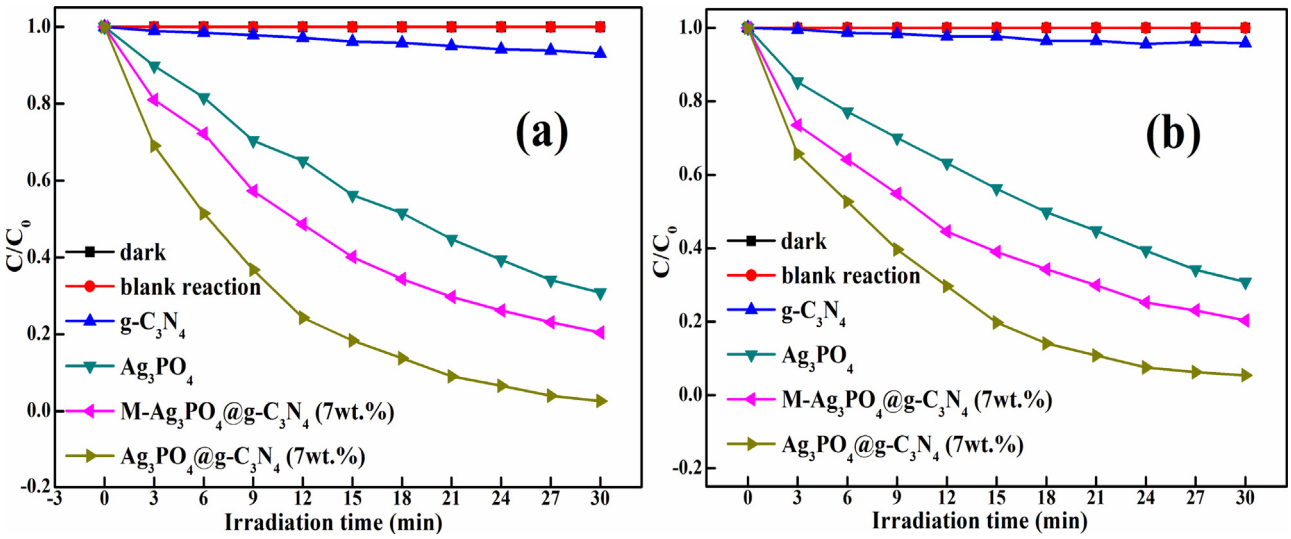

Fig. 7. Concentration changes of MB (a) and BPA (b) over various photocatalysts under visible light irradiation.

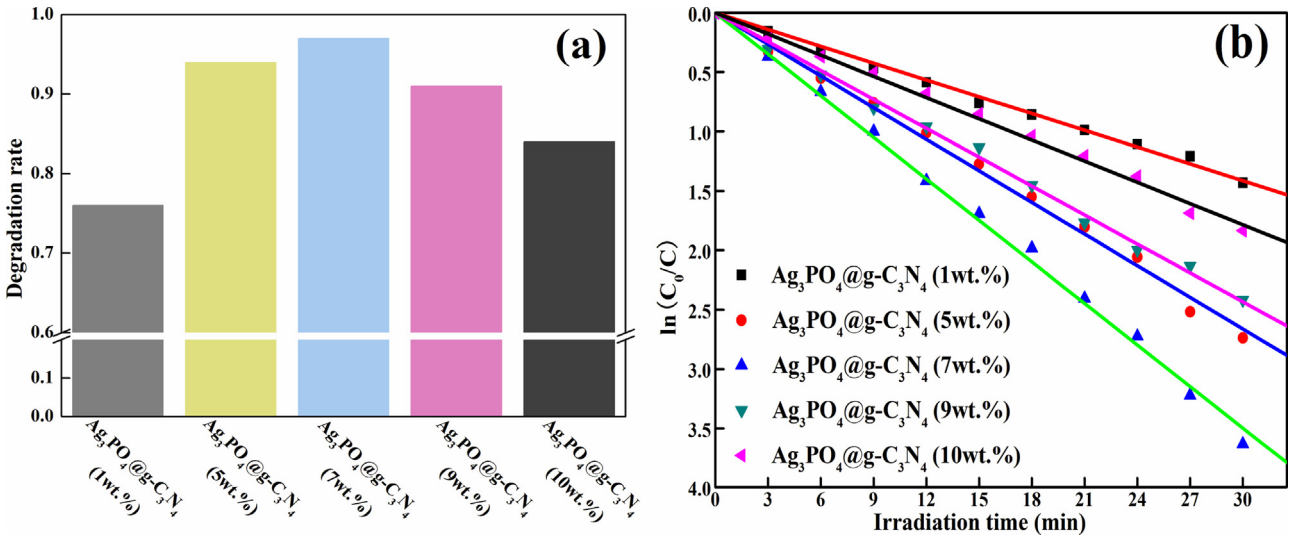

Fig. 8. Degradation rate (a) and first-order rate constant (b) of Ag_3PO_4@g-C_3N_4 composite with various g-C_3N_4 contents on degradation of MB.

structural stability of Ag_3PO_4@g-C_3N_4 for the photocatalytic reaction. To evaluate the structural stability, the crystalline structures of Ag_3PO_4@g-C_3N_4 nanocomposite before and after experiments were studied (as shown in Fig. 10). In the Fig. 10b, no extra characteristic diffraction peaks were observed in its XRD spectra pattern. So, no evident crystalline structure changes could be observed in the XRD pattern of Ag_3PO_4@g-C_3N_4 nanocomposite after photocatalytic reaction [10], indicating that the shell g-C_3N_4 improved the stability of the Ag_3PO_4 photocatalyst. The surface components and composition of Ag_3PO_4@g-C_3N_4 nanoparticles before and after photocatalytic reaction were investigated by XPS analysis. In Fig. 10c, the two peaks in the spectra of Ag_3PO_4 appearing at 373.96 and 367.97 eV could be ascribed to the binding energies of Ag $3d_{3/2}$ and Ag $3d_{5/2}$, respectively, of Ag^+ ions. After the photocatalytic reaction, the Ag $3d_{3/2}$ and Ag $3d_{5/2}$ peaks of Ag_3PO_4 showed no obvious decrease and shift. The result imply no obvious of metallic Ag was found in the process of photocatalytic reaction [4,37]. The result was also confirmed by TEM (Fig. 11) of the composite sample after reaction, which clearly showed no small Ag nanoparticles on the interface in Ag_3PO_4 with g-C_3N_4. Therefore, the incorporation of g-C_3N_4 with Ag_3PO_4 photocatalyst can not only enhance the visible light photocatalytic performance of Ag_3PO_4, but also inhibit the photo-corrosion and therefore, promote the stable-durability of its photocatalytic activity.

The separation efficiency of electrons and holes plays a vital role in the photocatalytic reaction. Photoelectrochemical parameters can be used to qualitatively study the excitation and transfer of photo-generated charge carriers in photocatalysts [38,39]. Fig. 12 shows the photocurrent density versus the irradiation time curve of the as-prepared samples under chopped illumination. It is clear that the photocurrent densities rapidly decreased to zero as soon as the lamp was turned off, and the photocurrents maintained stable values when the lamp was turned on. The Ag_3PO_4@g-C_3N_4 (7 wt.%) produced a much higher photocurrent than both Ag_3PO_4 and g-C_3N_4 under same condition, indicating a smaller recombination and a more efficient separation of photo-generated electron-hole pairs occurred at the interface between Ag_3PO_4 and g-C_3N_4 in the Ag_3PO_4@g-C_3N_4 composite.

Electrochemical impedance spectroscopy was used to investigate the charge transfer and recombination processes at solid/electrolyte interfaces in the photocatalyst [40,41]. The equivalent circuit (inset of Fig. 13) of the devices was constructed

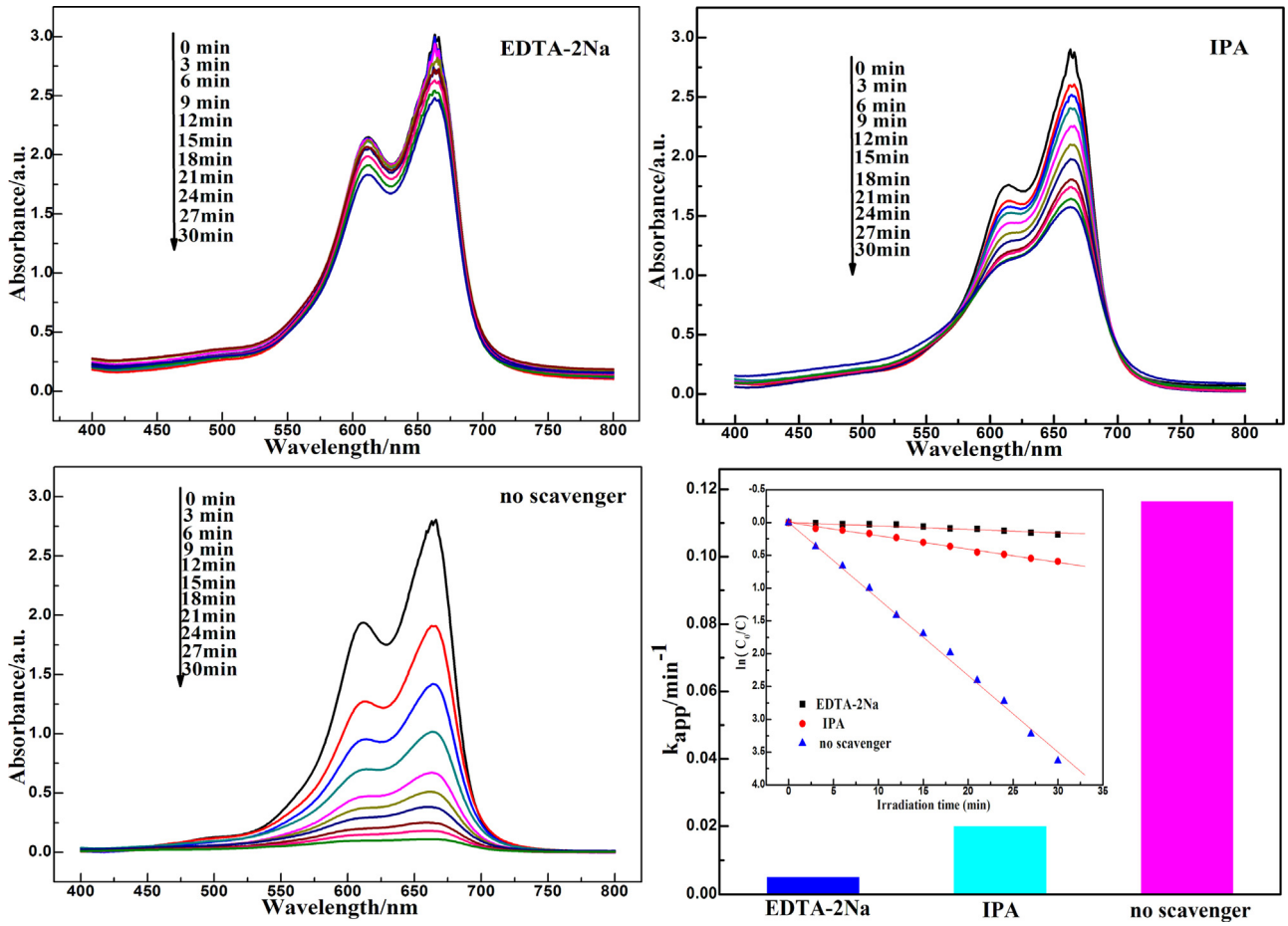

Fig. 9. Phaotocatalytic degradation of MB over Ag_3PO_4@g-C_3N_4 (7 wt.%) in the presence of EDTA-2Na, IPA and in the absence scavengers. The rate constants (k_{app}) are shown in (d).

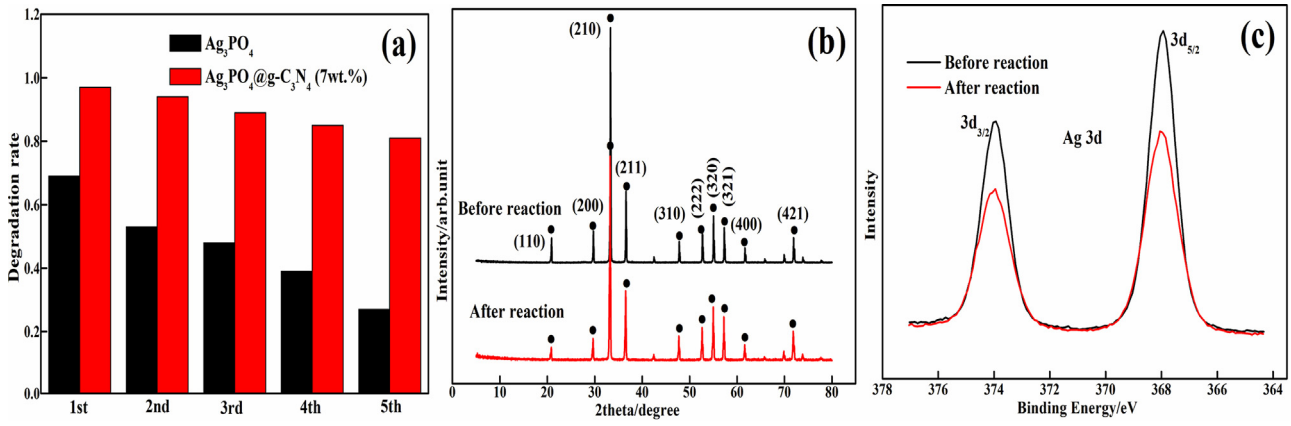

Fig. 10. Recycling runs (a) of the degradation of MB, XRD (b) and Ag 3d XPS spectra (c) before and after photocatalytic reaction.

to analyze the impedance spectra, and the impedance spectra were fitted by the ZSimpWin software. R_1 is the series resistance of the system. The first semi-circle (high frequency) can be assigned to the charge-transfer resistance (R_2) of the Pt counter electrode/electrolyte interface. The second semi-circle (middle frequency) can be assigned to the charge-transfer resistance (R_2) of the as prepared samples anode/electrolyte interface [42]. In Nyquist diagram, a smaller radius is an indication of an overall smaller charge transfer resistance or, equivalently, a more facile charge transfer process at the electrode/electrolyte interface. As shown in Fig. 13, the diameter of the arc radius on the EIS Nynquist plot of the Ag_3PO_4@g-C_3N_4 (7 wt.%) composite electrode is much smaller than those of the Ag_3PO_4 and g-C_3N_4 electrodes under visible light irradiation, indicating a more effective separation of photo-generated electron-hole pairs and fast interface charge transfer occurred in the Ag_3PO_4@g-C_3N_4 composites.

This novel photocatalyst Ag_3PO_4 exhibited high quantum efficiency under visible light irradiation. However, Ag_3PO_4 seriously suffers from photo-corrosion under strong illumination. Hence, enormous efforts have been dedicated to either reducing the recombination of photo-generated charge carriers or inhibiting the photocorrosion of Ag_3PO_4. Various coupled systems such as

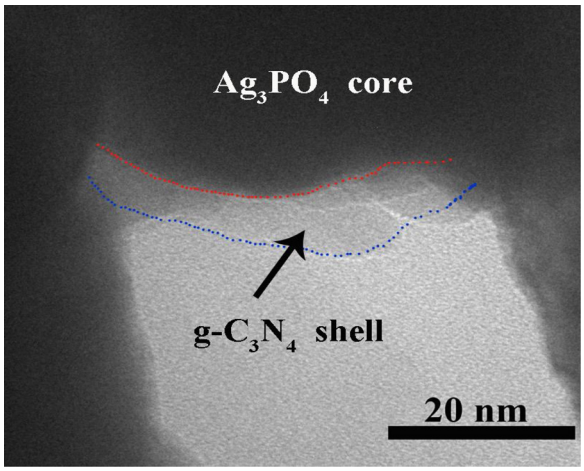

Fig. 11. TEM of Ag_3PO_4@g-C_3N_4 after photocatalytic reaction.

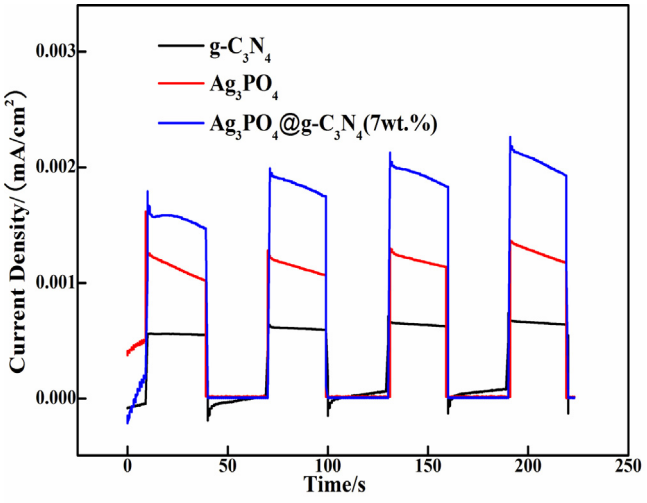

Fig. 12. Transient photocurrent of g-C_3N_4, Ag_3PO_4 and Ag_3PO_4@g-C_3N_4 under visible light irradiation.

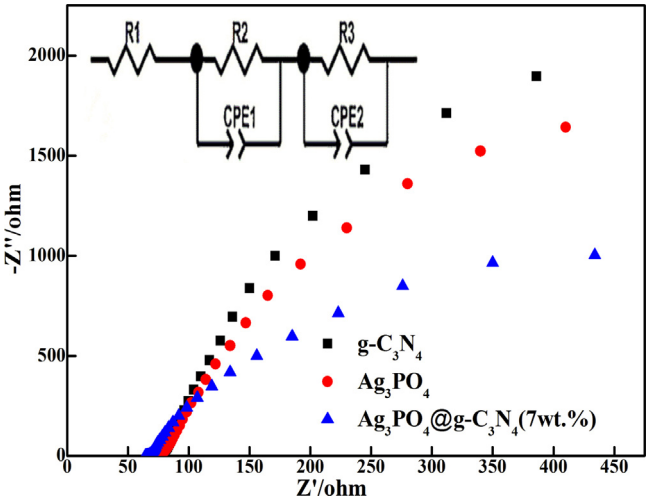

Fig. 13. The electrochemistry properties of Ag_3PO_4, g-C_3N_4 and Ag_3PO_4@g-C_3N_4 electrodes under visible light irradiation: impedance spectra with the corresponding equivalent circuit models.

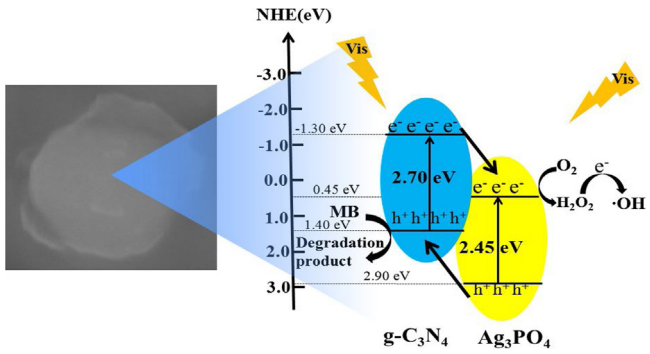

Fig. 14. Schematic illustration of the mechanism for the high photocatalytic performance of Ag_3PO_4@g-C_3N_4 composite.

Ag_3PO_4/TiO_2 [6], Ag_3PO_4/ZnO [7], Ag_3PO_4/g-C_3N_4 [10] can address the issue of photocorrosion by accelerating the separation of photo-generated charge carriers. Moreover, Ag_3PO_4 can be protected by being coated with graphene [16] to reduce photocorrosion. Whatever, g-C_3N_4 nano-sheets was not reported used in the shell for Ag_3PO_4. The novel structure core@shell can accelerate the separation of photo-generated charge carriers which is similar to those that have been well reported in the literature. And also, stable allotrope of carbon nitrides g-C_3N_4 can effectively protect Ag_3PO_4 from dissolution in the aqueous solution and avoid loss of silver phosphate. Compared with graphene, g-C_3N_4 can absorb the visible light and enhance photocatalytic activity dramatically combine with Ag_3PO_4 by suitable energy band structure. Based on the results of structure characterizations and the visible light photocatalytic tests of the as-prepared samples, a possible mechanism for the high photocatalytic performance of Ag_3PO_4@g-C_3N_4 composite in the degradation of MB is proposed and illustrated in Fig. 14. The g-C_3N_4 nano-sheets coated on the surface of Ag_3PO_4 nanoparticles can effectively protect it from dissolution in the aqueous solution. The driving force for charge transfer is known to originate from the matched band potentials between two semiconductors. The intense interaction existed between g-C_3N_4 and Ag_3PO_4 was essential to promoting the separation efficiency of photo-generated carriers. It is well known that both Ag_3PO_4 and g-C_3N_4 can be excited to generate electrons and holes under visible light irradiation. The LUMO and HOMO potentials of g-C_3N_4 are -1.4 and 1.3 eV, respectively, and CB and VB of Ag_3PO_4 are 0.45 and 2.9 eV, respectively [4,43]. The LUMO potential of g-C_3N_4 is more negative than CB of Ag_3PO_4. The photo-generated electrons of g-C_3N_4 can be directly injected into the CB of Ag_3PO_4 through the well-defined interface. The photo-induced electrons can diffuse to the surface and reacted with the oxygen molecule that is a well-known electron acceptor, generating •OH. The •OH are of high oxidation activity, which can decompose MB. As depicted in Fig. 14, the excited holes produced by Ag_3PO_4 are injected into the HOMO of g-C_3N_4 and the photo-generated holes are collected in the HOMO of g-C_3N_4. The photo-induced holes can diffuse to the surface and act as the main active species for the photocatalytic degradation. The charge transfer effectively inhibits the recombination of photo-generated electron-hole pairs and thus enhances the photocatalytic activity.

4. Conclusion

A novel Ag_3PO_4@g-C_3N_4 core@shell composite photocatalyst was prepared and its photocatalytic performance was investigated. The results indicate that the introduction of g-C_3N_4 can significantly improve the visible-light responsive photocatalytic activity of the Ag_3PO_4 photocatalyst and the content of g-C_3N_4 can

significantly affect its photocatalytic performance. The optimal g-C_3N_4 content was found to be 7.0 wt%. The deep photo-oxidation activities for degradation of MB and bisphenol A over Ag_3PO_4@g-C_3N_4 composite photocatalyst reached 97% and 94.6%, which were respectively 1.4 and 1.7 times of those of bulk Ag_3PO_4. The matched energy level between g-C_3N_4 and Ag_3PO_4 leads to the efficient separation and transfer of photo-generated electron-hole at their interface, improving the photocatalytic performance of Ag_3PO_4@g-C_3N_4 composite. In addition, g-C_3N_4 shell can protect Ag_3PO_4 nanoparticles from dissolution during the photocatalytic reaction, leading to a high stability of the Ag_3PO_4@g-C_3N_4 composite photocatalyst. In conclusion, Ag_3PO_4@g-C_3N_4 composite is a promising photocatalyst for the removal of organic pollutants in the environmental protection.

Acknowledgements

This work was financially supported by the National Natural Science Foundation of China (No. 51372068), Hebei Natural Science Funds for Distinguished Young Scholar (No. B2014209304).

References

[1] M.N. Chong, B. Jin, C.W.K. Chow, C. Saint, Water Res. 44 (2010) 2997–3027.
[2] R. Daghrir, P. Drogui, D. Robert, Ind. Eng. Chem. Res. 52 (2013) 3581–3599.
[3] X.J. Wang, W.Y. Yang, F.T. Li, Y.B. Xue, R.H. Liu, Y.J. Hao, Ind. Eng. Chem. Res. 52 (2013) 17140–17150.
[4] J.W. Xu, Z.D. Gao, K. Han, Y.M. Liu, Y.Y. Song, ACS Appl. Mater. Interfaces 6 (2014) 15122–15131.
[5] Z.H. Chen, W.L. Wang, Z.G. Zhang, X.M. Fang, J. Phys. Chem. C 117 (2013) 19346–19352.
[6] W. Yao, B. Zhang, C. Huang, C. Ma, X. Song, Q. Xu, J. Mater. Chem. 22 (2012) 4050–4055.
[7] C. Dong, K.L. Wu, M.R. Li, L. Liu, X.W. Wei, Catal. Commun. 46 (2014) 32–35.
[8] C. Cui, Y.P. Wang, D.Y. Liang, W. Cui, H.H. Hu, B.Q. Lu, S. Xu, X.Y. Li, C. Wang, Y. Yang, Appl. Catal. B: Environ. 158–159 (2014) 150–160.
[9] J.H. Liu, X. Li, F. Liu, L.H. Lu, L. Xu, L.W. Liu, W. Chen, L.M. Duan, Z.R. Liu, Catal. Commun. 46 (2014) 138–141.
[10] Q.J. Xiang, D. Lang, T.T. Shen, F. Liu, Appl. Catal. B: Environ. 162 (2015) 196–203.
[11] P.Y. Dong, Y.H. Wang, B.C. Cao, S.Y. Xin, L.N. Guo, J. Zhang, F.H. Li, Appl. Catal. B: Environ. 132–133 (2013) 45–53.
[12] H. Katsumata, T. Sakai, T. Suzuki, S. Kaneco, Ind. Eng. Chem. Res. 53 (2014) 8018–8025.
[13] B. Chai, F.Y. Zou, W.J. Chen, J. Mater. Res. 30 (2015) 1128–1136.
[14] C.S. Pan, J. Xu, Y.J. Wang, D. Li, Y.F. Zhu, Adv. Funct. Mater. 22 (2012) 1518–1524.
[15] S. Khanchandani, S. Kundu, A. Patra, A.K. Ganguli, J. Phys. Chem. C 116 (2012) 23653–23662.
[16] D.M. Chen, K.W. Wang, D.G. Xiang, R.L. Zong, W.Q. Yao, Y.F. Zhu, Appl. Catal. B: Environ. 147 (2014) 554–561.
[17] L. Liu, J.C. Liu, D.D. Sun, Catal. Sci. Technol. 2 (2012) 2525–2532.
[18] X.C. Wang, K. Maeda, A. Thomas, K. Takanabe, G. Xin, J.M. Carlsson, K. Domen, A. Markus, Nat. Mater. 8 (2009) 76–80.
[19] Y. Wang, X.C. Wang, M. Antonietti, Angew. Chem. Int. Ed. 51 (2012) 68–89.
[20] J.Y. Zhang, Y.H. Wang, J. Jin, J. Zhang, Z. Lin, F. Huang, J.G. Yu, ACS Appl. Mater. Interfaces 5 (2013) 10317–10324.
[21] S. Kumar, A. Baruah, S. Tonda, B. Kumar, V. Shanker, B. Sreedhar, Nanoscale 6 (2014) 4830–4842.
[22] X.J. Bai, R.L. Zong, C.X. Li, D. Liu, Y.F. Liu, Y.F. Zhu, Appl. Catal. B: Environ. 147 (2014) 82–91.
[23] G.Z. Liao, S. Chen, X. Quan, H.T. Yu, H.M. Zhao, J. Mater. Chem. 22 (2012) 2721–2726.
[24] X.D. Zhang, X. Xie, H. Wang, J.J. Zhang, B.C. Pan, Y. Xie, J. Am. Chem. Soc. 135 (2013) 18–21.
[25] B.J. Jiang, Y.H. Wang, J.Q. Wang, C.G. Tian, W.J. Li, Q.M. Feng, Q.J. Pan, H.G. Fu, ChemCatChem 5 (2013) 1359–1367.
[26] Z.W. Tong, D. Yang, Y.Y. Sun, Y. Tian, Z.Y. Jiang, Phys. Chem. Chem. Phys. 17 (2015) 12199–12206.
[27] J.S. Zhang, M.W. Zhang, C. Yang, X.C. Wang, Adv. Mater. 26 (2014) 4121–4126.
[28] P.Y. Dong, Y.H. Wang, H.H. Li, H. Li, X.L. Ma, L.L. Han, J. Mater. Chem. A 1 (2013) 4651–4656.
[29] Z.L. Xiu, H. Bo, Y.Z. Wu, X.P. Hao, Appl. Surf. Sci. 289 (2014) 394–399.
[30] M. Thomas, S.K. Ghosh, K.C. George, Mater. Lett. 56 (2002) 386–392.
[31] S.C. Yan, Z.S. Li, Z.G. Zou, Langmuir 25 (2009) 10397–10401.
[32] H. Zhang, R.L. Zong, Y.F. Zhu, J. Phys. Chem. C 113 (2009) 4605–4611.
[33] Y.J. Wang, Z.X. Wang, S. Muhammad, J. He, CrystEngComm 14 (2012) 5065–5070.
[34] X.G. Ma, B. Lu, D. Li, R. Shi, C.S. Pan, Y.F. Zhu, J. Phys. Chem. C 115 (2011) 4680–4687.
[35] P.Y. Dong, Y.H. Wang, B.C. Cao, S.Y. Xin, L.N. Guo, J. Zhang, F.H. Li, Appl. Catal. B: Environ. 132–133 (2013) 45–53.
[36] S.W. Hu, L.W. Yang, Y. Tian, X.L. Wei, J.W. Ding, J.X. Zhong, P.K. Chu, Appl. Catal. B: Environ. 163 (2015) 611–622.
[37] X.J. Guan, L.J. Guo, ACS Catal. 4 (2014) 3020–3026.
[38] J.G. Yu, G.P. Dai, B. Cheng, J. Phys. Chem. C 114 (2010) 19378–19385.
[39] N. Zhang, S.Q. Liu, X.Z. Fu, Y.J. Xu, J. Mater. Chem. 22 (2012) 5042–5052.
[40] S. Yang, Y. Gong, J. Zhang, L. Zhan, L. Ma, Z. Fang, R. Vajtai, X. Wang, P.M. Ajayan, Adv. Mater. 25 (2013) 2452–2456.
[41] L.Y. Huang, H. Xu, Y.P. Li, H.M. Li, X.N. Cheng, J.X. Xia, Y.G. Xu, G.B. Cai, Dalton Trans. 42 (2013) 8606–8616.
[42] L. Wang, B.X. Han, L. Dai, H.Z. Zhou, Y.H. Li, Y.L. Wu, J. Zhu, J. Hazard Mater. 262 (2015) 545–553.
[43] Q.J. Xiang, J.G. Yu, M. Jaroniec, J. Phys. Chem. C 115 (2011) 7355–7363.